RESEARCH PAPER

Thermomechanical Analysis and Optimization of Residual Stresses in SS316L Components Fabricated by Directed Energy Deposition

Farnoosh Turki*, Abdolhossein Jalali Aghchai

* *farnoosh.turki@email.kntu.ac.ir*

Faculty of Mechanical Engineering, K.N. Toosi University of Technology, Tehran, Iran

Received: January 2026 **Revised: May 2026** **Accepted: July 2026**
DOI: 10.22068/ijmse.4534

Abstract: *The Directed Energy Deposition (DED) process is highly sensitive to thermal conditions and tends to produce residual stresses and geometric distortion. It is important to understand the influence of processing parameters on these effects in order to enhance build quality. The objective of this study is to control residual stress and distortion in the DED process by investigating baseplate thickness, number of layers deposited before laser interruption, dwell time, and laser power using a full factorial experiment design. The numerical results were validated by experimental residual stress measurements using the X-ray diffraction (XRD) technique. The optimized processing conditions resulted in a 43% reduction in residual stress and a 33% decrease in dimensional distortion compared to the baseline setup. Among the four factors, baseplate thickness had the most significant effect, whereas dwell time had the least impact. To the best of the authors' knowledge, the combined effect of baseplate thickness, dwell time, number of layers deposited before laser interruption, and laser power on residual stress and distortion in DED has not been previously investigated. The findings of this study provide a mathematical basis for future research aimed at optimizing process and material parameters in the DED process.*

Keywords: *Direct energy deposition, Residual stress, Thermal-mechanical modeling, Optimization, SS316L.*

1. INTRODUCTION

Additive Manufacturing (AM), also referred to as additive layer-wise fabrication technology, has revolutionized the manufacturing of complex geometries and bespoke components across a multitude of industrial sectors, including aeronautical engineering, biomedicine, and automotive manufacturing. Among the spectrum of additive manufacturing modalities, DED distinguishes itself through its capacity to fabricate large-volume metallic alloys via concentrated thermal energy delivery systems, such as focused laser, plasma arc, or electron beams, enabling high material deposition rates and improved material utilization efficiency [1, 2]. Despite these advantages, DED processes inherently involve significant thermal gradients and rapid solidification rates, which can induce residual stresses within the fabricated components [3, 4]. These residual stresses may negatively impact the mechanical performance, dimensional accuracy, and overall structural integrity of the parts, potentially resulting in early failure or deformation [5, 6]. It is essential to understand and predict residual stress development in DED to optimize process parameters and guarantee the reliability of the produced parts. Several modeling techniques have been employed to simulate the thermal and mechanical behavior of DED, such as finite element analysis (FEA), analytical models, and computational fluid dynamics (CFD) simulations [7, 9]. Thermal modeling typically employs heat source models, i.e., the Goldak double ellipsoidal model, to model the temperature distribution that occurs during deposition [10, 11], mechanical models generally focus on the stress and strain history accumulated as a result of thermal cycles, phase transformations, and material properties [12, 13].

Empirical validation of such models is necessary to determine their validity and usefulness. Measurement techniques such as X-ray diffraction (XRD), neutron diffraction, and hole-drilling are commonly applied in measuring residual stresses in parts produced by directed energy deposition [14]. Various methods of minimizing residual stresses in DED have been investigated in current research, including substrate preheating, scanning strategy optimization, and the application of interlayer dwell times [15, 16]. Moreover, the influence of process parameters such as laser power, scanning speed, and layer thickness on the development of residual stress has been well studied in the literature [17-20]. Developments in the field of materials science have also helped in controlling residual stress. The incorporation of functionally graded materials and the introduction of alloying constituents have shown promise in minimizing residual stress levels [21, 22]. Although these efforts have been attempted,

difficulties remain in accurately predicting and controlling residual stresses in the DED processes. The complex coupling of thermal cycles, material response, and process parameters necessitates additional studies to formulate thorough models and effective mitigation measures [23].

This study aims to develop a thermomechanical 3D transient model to simulate distortion, temperature history, and residual stresses in DED parts fabricated from SS316L. The model employs the Goldak heat source representation and also considers various process parameters such as laser power, dwell time, number of layers deposited before laser shutdown (layer count), and baseplate thickness. Experimental validation is performed using XRD measurements to determine the validity of the model. In addition, the process and material parameters are optimized to reduce residual stresses and distortion.

2. EXPERIMENTAL PROCEDURES

2.1. Experimental Setup

The Directed Energy Deposition system employed in the current work is schematically illustrated in Figure 1(a). It comprises a YB: YAG laser with an operating wavelength of 1080 nm and a power output of 1000 W, a sealed build chamber featuring a built-in nozzle and circuit control unit, a laser stabilizer, and a closed-loop chiller capable of providing stable thermal conditions. The powder delivery mechanism is a coaxial dual-chamber feeder (Figure 1b), ensuring a consistent supply of powder for deposition. Argon was utilized as the carrier and shield gas to minimize oxidation.

Table 1 presents the geometrical and process parameters selected for the initial deposition pass in the DED process.

The experimental wall was fabricated by stacking a single deposition pass over sixteen successive layers. The printing direction corresponds to the X-axis, while the Z-axis represents the build direction through the thickness of the part.

The SS316L powder used in this study was supplied by Hermos GmbH (Germany). According to the manufacturer's technical datasheet, the powder was produced via gas atomization and exhibited a nearly spherical morphology with a particle size distribution ranging from 45 µm to 105 µm. The provided specifications were used as input data for thermal and material modeling.

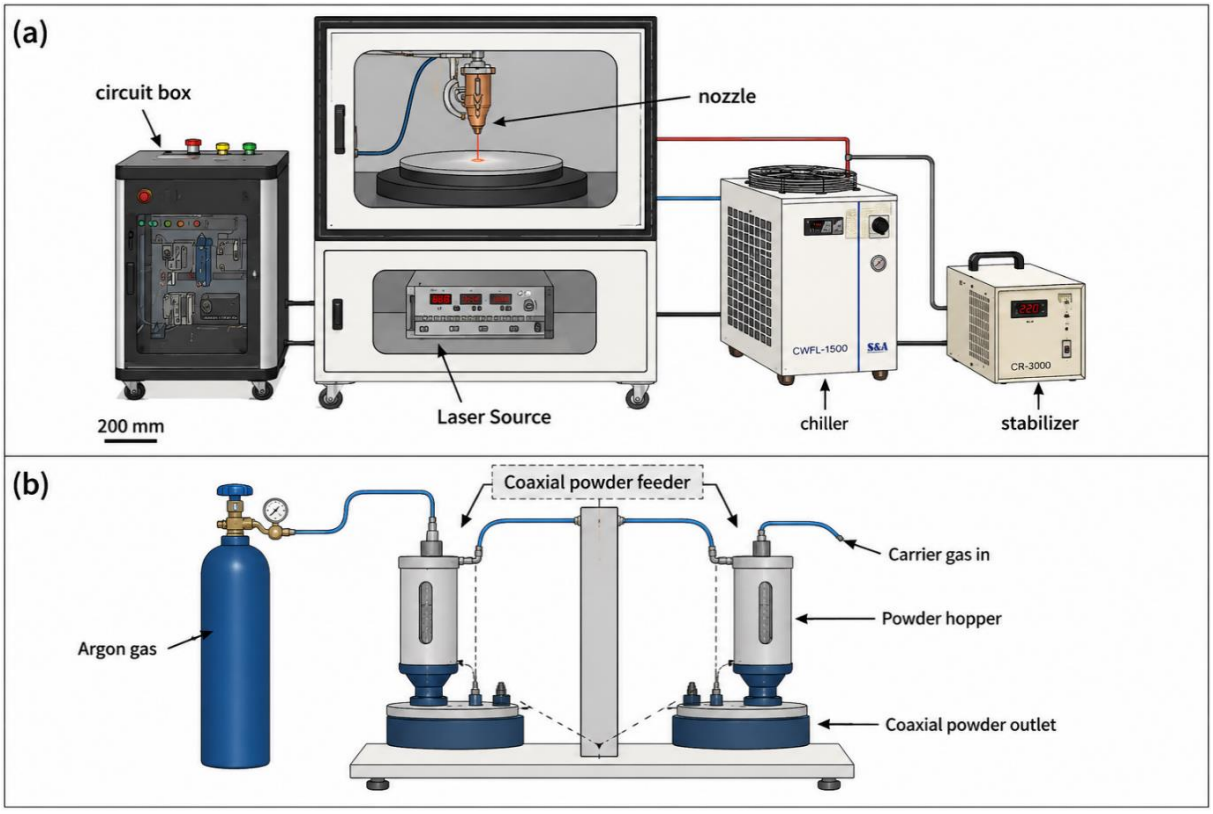

Fig. 1. a) Experimental setup showing the laser source, chiller, stabilizer, circuit box, and nozzle. b) Coaxial powder feeder used for powder delivery in the DED process

Table 1. Geometrical and process parameters considered for the deposition process

Nozzle speed (mm/s)	Laser power (W)	Powder feed rate (g/min)	Nozzle distance from the baseplate (mm)	The average pass height (mm)	Average pass width (mm)
10	1000	6.4	12	0.31	1.25

2.2. Finite Element Simulation

In the present study, a two-step finite element simulation was used to simulate the development of residual stresses in parts produced by the DED process. Numerical simulations were conducted in all cases using ABAQUS version 6.13, following a sequential thermal-mechanical method. The initial step consisted of a transient thermal solution to capture the temperature history of the domain, which was subsequently used as input in the second step to compute thermally induced stresses.

2.2.1. Geometry and mesh

The simulated geometry comprised a rectangular 316L stainless steel baseplate and a deposited wall. The baseplate length was 22.18 mm, and the deposited wall dimensions were 33.5 mm (length) × 1.25 mm (width) × 5 mm (height). All parts were discretized using structured 8-node linear brick elements (C3D8T) for the thermal simulation, followed by conversion to C3D8 elements for mechanical analysis (Figure 2).

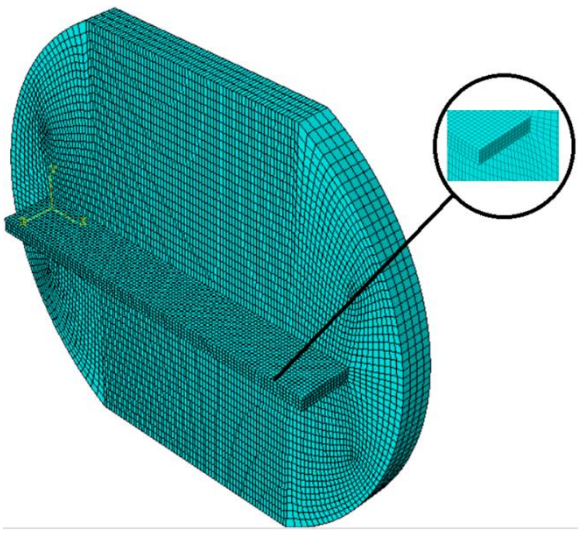

Fig. 2. Finite element mesh of the wall-type structure deposited on a circular baseplate

For spatial accuracy and computational efficiency, 34,226 elements were employed.

2.2.2. Thermal simulation

The transient heat transfer was modeled using a Goldak double ellipsoidal heat source, which is appropriate for simulating energy input in laser-based DED. The heat source was defined with spatial and temporal parameters to reflect the actual deposition path. The governing heat conduction equation in three dimensions is:

$$Q + (\lambda \nabla T).\nabla = \frac{\partial T}{\partial t}\ \rho C_p \quad (1)$$

Where T is temperature, λ is thermal conductivity, ρ is density, C_p is specific heat capacity, and Q is the internal heat generation defined by the laser. Boundary conditions included convection and radiation losses applied to all free surfaces using a film coefficient of h= 4 $W/m^2 \cdot K$ and emissivity ϵ= 0.75. The initial temperature was set at 298 K. Material was added in layers using the element activation technique (Model Change interaction). Inactive elements were thermally initialized but not included in the heat transfer solution until their corresponding deposition step. The thermal input was applied using a user-defined DFLUX subroutine in ABAQUS, written in Python, to implement the moving heat source based on the Goldak double-ellipsoidal model.

2.2.3. Mechanical simulation

After the thermal step, the resulting temperature history was mapped into a separate mechanical step using the initial conditions and Predefined Field tools. The mechanical behavior of the material included temperature-dependent elastic–plastic deformation with isotropic hardening. The total strain was decomposed as:

$$\varepsilon_{thermal} + \varepsilon_{plastic} + \varepsilon_{elastic} = \varepsilon_{total} \quad (2)$$

with thermal strain given by Equation 3.

$$\varepsilon_{thermal} = \alpha \Delta T \quad (3)$$

In Equation 3, α is the thermal expansion coefficient and ΔT represents the temperature difference between the deposition temperature and the reference temperature. The bottom face of the baseplate was fully fixed in all degrees of freedom to replicate clamping. A final unclamping step was added to reflect stress redistribution upon fixture release. The mechanical and thermal properties used in the numerical simulations were taken from [24].

2.2.4. Residual stress measurement

Experimental confirmation of the numerical findings was conducted using XRD. The $\sin^2(\psi)$ technique

was employed to measure the surface residual stresses in the constructed wall. The diffraction peak of the (311) plane of the austenitic γ-Fe phase was examined with Cu-Kα radiation (λ= 1.5405980 Å), and the scan parameters are listed in Table 2.

Table 2. Parameters used for residual stress measurement using X-ray diffraction (XRD)

Parameters	Value
2θ Range	89.025°–92.475°
Focus type	Line (12 × 0.4 mm)
Voltage/current	40 kV/30 mA
Step size	0.05°
Tilt range	–5° to + 5°
Scanning speed	0.0244°/s

Residual stress was determined by plotting the measured d-spacing values versus $\sin^2(\psi)$ and applying linear regression according to Equation 4, where the slope of the fitted line (m) is directly related to the residual stress.

$$d = m \times \sin^2(\psi) + d_0 \quad (4)$$

Residual stress (σ) was calculated using Equation 5:

$$\sigma = \frac{m}{d_0} \cdot \frac{E}{\nu+1} \quad (5)$$

where E= 193 GPa is Young's modulus, ν= 0.27 is Poisson's ratio, and d_0= 1.08588 Å is the stress-free lattice spacing. The linear slope m was obtained from the regression of d-spacing versus $\sin^2(\psi)$. The numerical and experimental results were compared at a location 3 mm above the baseplate, where thermal gradients were most significant. The validated model was then used for parametric optimization of the DED process.

3. RESULTS AND DISCUSSION

3.1. Residual Stress Evaluation via XRD and FEM Validation

Figure 3 illustrates the XRD analysis conducted on the additively manufactured SS316L wall using the DED process. The diffraction pattern exhibits strong peaks of the austenitic γ-Fe phase, namely the (111), (200), and (311) crystallographic planes, confirming the formation of a face-centered cubic (FCC) microstructure typical of SS316L. Minor peaks associated with the δ-ferrite phase, such as δ (110) and δ (200), are also present, indicating partial phase transformation due to high thermal gradients during layer-wise deposition. The residual stress was determined using the standard $\sin^2\psi$ method on the (311) peak, located around 2θ≈ 90.35°. The magnified inset shows that linear regression analysis of d-spacing versus $\sin^2\psi$ gave a compressive stress value of approximately −72 MPa at a position approximately 3.8 mm above the baseplate. This location was in a region of large thermal gradients due to the rapid cooling effect of the substrate.

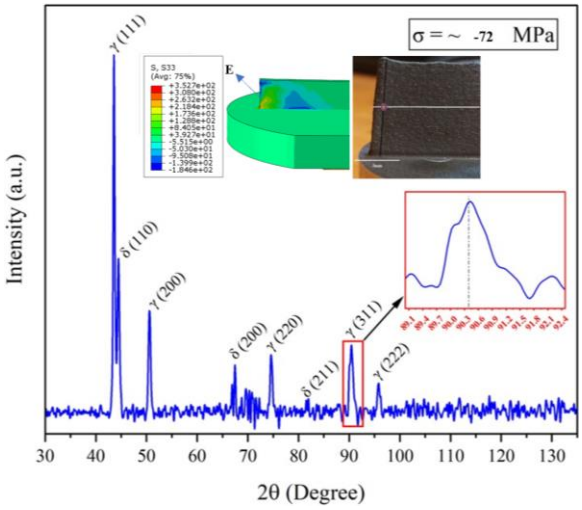

Fig. 3. XRD pattern of the fabricated SS316L sample, showing dominant peaks of γ-Fe and δ-Fe phases. The (311) peak used for residual stress calculation is highlighted. Inset figures show: (top-left) simulated residual stress distribution (S33), (top-right) photograph of the fabricated wall, and (bottom-right) extracted (311) peak profile for $\sin^2\psi$ analysis

For numerical model verification, a thermo-mechanical coupled finite element model was employed in ABAQUS to simulate the same position. The simulation resulted in an estimated residual stress of about −73.4 MPa in the vertical direction (S33), indicating good agreement with the experimental result. The relative error obtained was less than 2%, thereby validating the accuracy of both the Goldak-based heat source model and the layer-wise element activation strategy employed in the numerical model. The localized compressive stress at this height can be attributed to constrained contraction during cooling, where the previously deposited and partially reheated layers restrict shrinkage and promote compressive stress development near the measured region. Such a high correlation verifies that the numerical model developed can effectively simulate the development of residual stress and be experimentally validated using XRD, which provides greater confidence in subsequent parametric analysis and optimization processes.

3.2. Effect of Process Parameters on Average Residual Stress

Table 3 presents the average residual stress values

obtained from 16 different simulation cases based on a full factorial design, involving four primary process parameters: laser power (800 W, 1200 W), dwell time (200 s, 400 s), number of layers (2, 4), and baseplate thickness (3 mm, 5 mm).

The lower residual stress observed in the 5 mm baseplate cases suggests that increasing baseplate thickness improves thermal stiffness and heat dissipation capacity, thereby reducing thermal gradients and stress accumulation during deposition. These results were used as input data for the statistical analysis and for modeling of parameter effects in the DED process. Table 4 presents the analysis of variance (ANOVA) results for residual stress.

Table 4 shows the quantitative contribution of each process parameter to the variation in residual stress based on the analysis of variance. The most influential individual factor was baseplate thickness (BT), contributing approximately 8.2% to the total variance. Although this contribution may appear small, it is statistically significant ($p < 0.001$), confirming BT as a dominant factor.

The interaction effect between BT and laser power (BT × P) was also significant, accounting for about 1.3% of the variance and showing high statistical significance ($p < 0.001$). In contrast, the number of layers (L) had a negligible effect (~0.003%, $p = 0.527$), demonstrating that it is not an influential parameter in residual stress determination among the parameters considered. The significance of the BT × P interaction indicates that the effect of laser power on residual stress is strongly dependent on the thermal constraint and heat-sink capacity provided by the baseplate thickness.

Table 3. Average residual stress (MPa) under various combinations of laser power, dwell time, layer count, and baseplate thickness

Parameters					Measurement of characteristics
Row	**Laser power (W)**	**Dwell time (s)**	**Layer count**	**Baseplate thickness (mm)**	**Average residual stress (MPa)**
1	800	200	2	3	147.707
2	1200	200	2	3	162.979
3	800	400	2	3	150.686
4	1200	400	2	3	167.271
5	800	200	4	3	152.525
6	1200	200	4	3	171.505
7	800	400	4	3	153.961
8	1200	400	4	3	172.017
9	800	200	2	5	98.816
10	1200	200	2	5	124.803
11	800	400	2	5	100.155
12	1200	400	2	5	127.698
13	800	200	4	5	100.628
14	1200	200	4	5	132.523
15	800	400	4	5	102.445
16	1200	400	4	5	133.260

Table 4. Results of the analysis of variance (ANOVA) for residual stress

Variable	Adj SS	Df	Adj MS	F-value	P-value
Regression	10432.8	7	1490.40	2520.13	0.000
BT	851.2	1	851.19	1439.29	0.000
L	0.3	1	0.26	0.44	0.527
DT	8.6	1	8.56	14.48	0.005
P	5.4	1	5.39	9.11	0.017
BT × P	140.1	1	140.11	236.91	0.000
L × DT	3.1	1	3.07	5.18	0.052
L × P	12.9	1	12.89	21.79	0.002
Error	4.7	8	0.59	1439.29	0.000
Total	10437.5	15	851.19	0.44	0.527
S= 0.76, R-sq= 99.95%, R-sq (adj)= 99.92%, R-sq (pred)= 99.82%					

Dwell time (DT) and laser power (P) individually contributed non-significantly by approximately ~0.08% and ~0.05%, respectively; however, both parameters were statistically significant because of the small residual error and high model sensitivity. The extremely low residual error of roughly 0.045% together with the high coefficients of determination (R^2= 99.95%, R^2 adj= 99.92%) guarantees the stability of the model and the appropriateness of the applied parameters. Figure 4 illustrates the main effects plot for residual stress optimization.

The highlighted red boxes indicate the selected optimal levels for each parameter, corresponding to a minimum predicted residual stress of 97.55 MPa. The high model accuracy is confirmed by the desirability value of 1.0000, indicating a perfect fit between the predicted and actual responses. Figure 5 presents the layer-by-layer thermal distribution (NT11) across the 16 deposition layers simulated under optimized conditions in the DED process. As shown in Figure 4, the optimal condition for minimizing residual stress (baseplate thickness= 5 mm, power= 800 W, dwell time= 200 s, layer count= 2) corresponds to Row 9 in Table 3. The steep negative slope observed for baseplate thickness further confirms that enhancing the thermal mass of the substrate is the dominant mechanism for lowering residual stress, whereas dwell time and layer count show comparatively weaker effects within the investigated parameter range. The slight difference between these values arises from the fact that the optimization result is based on a regression model fitted to all simulation data, while Table 3 contains discrete outputs from individual simulation runs.

In Figure 5, as the laser advances, a moving, distinct melt pool is created and grows with each consecutively deposited layer. A localized high-temperature region (in red to yellow), indicative of the melt pool zone, is symmetric and maintains a consistent shape throughout the build within the temperature profile. Heat penetration into the already deposited material is clearly observed, indicating good thermal bonding and consolidation. The melt pool width is quite consistent throughout the layers and is consistent with the predicted experimental width, thereby validating the accuracy of the laser heat input simulation. The observed increase in the temperature range in the higher layers also indicates cumulative thermal effects and reduced heat dissipation efficiency due to the structure's growing height. The findings validate that the simulation effectively incorporates transient thermal dynamics, thereby allowing for accurate prediction of melt pool expansion and its effect on structural integrity during the additive manufacturing process. The temperature profile obtained in this study follows the typical thermal distribution pattern observed in previous works, such as Yang et al. (2016), where similar thermo-mechanical behavior was reported for directed energy deposition processes [25]. The progressive enlargement of the thermally affected zone from lower to upper layers indicates heat accumulation during multi-layer deposition, which reduces the cooling rate and promotes a more gradual redistribution of thermal stresses in the deposited wall.

Figure 6 presents the distribution of residual stresses in the longitudinal (S11) and transverse (S22) directions for two different deposition stages, obtained from the coupled thermomechanical simulation of the DED process.

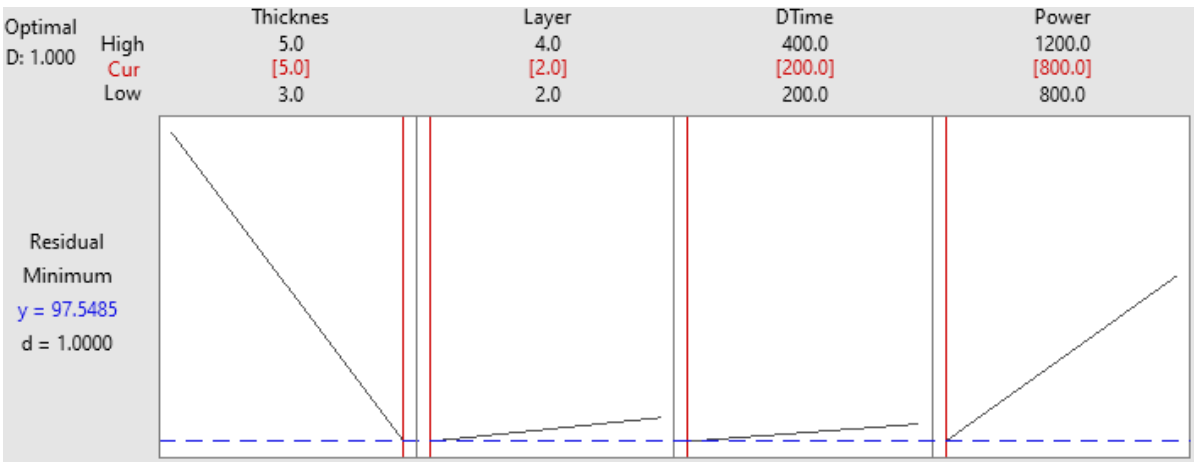

Fig. 4. Optimization plot for residual stress based on the DOE regression model, showing the predicted minimum stress (97.5 MPa) and the optimal levels of baseplate thickness (5 mm), layer count (2), dwell time (200 s), and laser power (800 W)

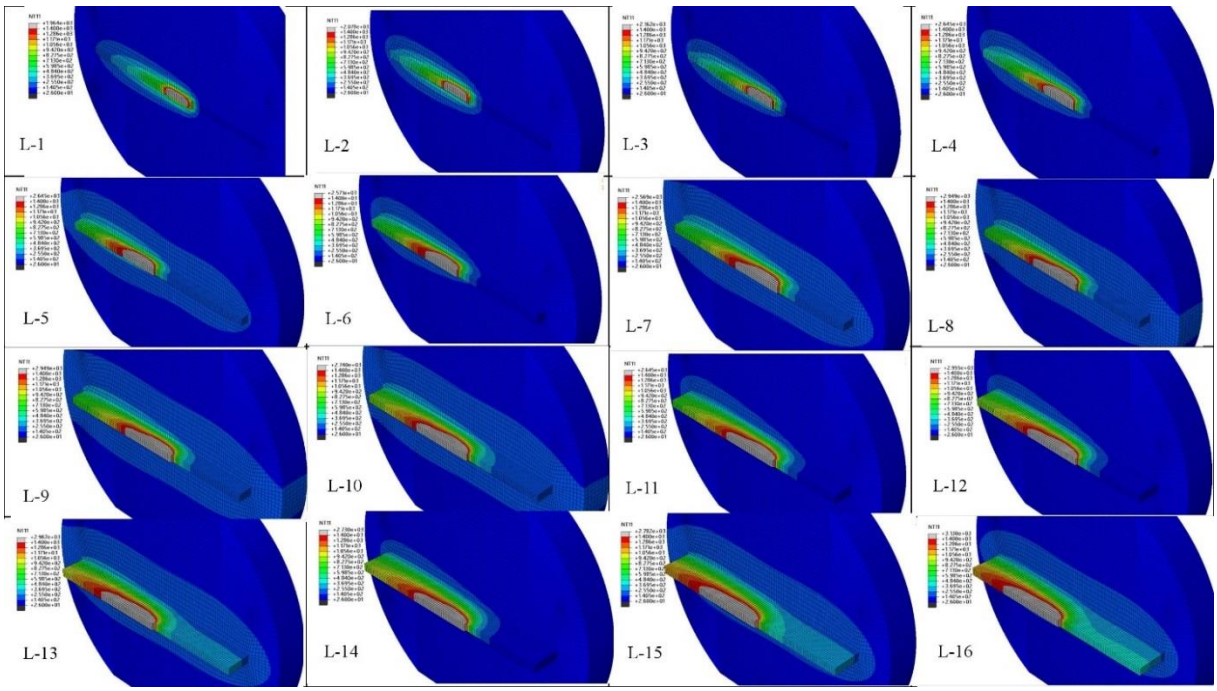

Fig. 5. Temperature distribution across 16 deposited layers

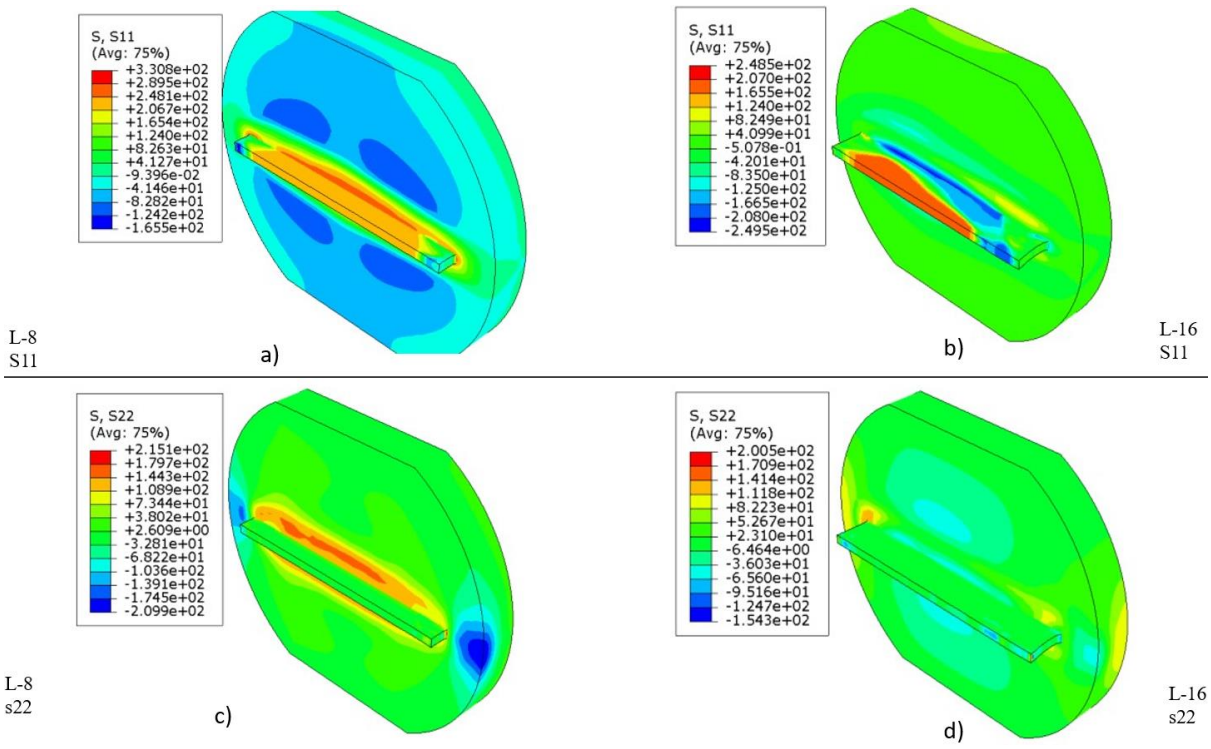

Fig. 6. Comparison of longitudinal (S11) and transverse (S22) residual stress distributions between layer 8 (a, c) and layer 16 (b, d)

As observed in Figure 6(a), at layer 8, the longitudinal residual stress shows a high tensile stress concentration toward the center of the deposited wall, with values greater than +300 MPa. This high stress value can partly be attributed to the intense thermal gradients and fast solidification that occur during the initial phases of deposition. However, in layer 16 (Figure 6(b)), the stress distribution is more uniform, and the peak values are considerably reduced, indicating thermal stress relaxation through successive layer

deposition and incremental heat build-up. At layer 8 (Figure 6(c)), the S22 stress field shows localized tensile stresses in the midsection of the wall. As deposition proceeds to layer 16 (Figure 6(d)), these stresses are significantly reduced and more uniformly distributed within the part, reflecting improved thermal balance and lower residual stress formation in the final layers. The study validates that an increase in the number of layers results in more homogeneous heat distribution, reduced thermal gradients, and therefore a significant reduction in residual stress values. Figure 7 shows the vertical displacement (U3) distribution for two different baseplate thicknesses.

Figure 7 compares the vertical displacement (U3) distributions for two representative runs:

- Run 9 (Figure 7(a)) corresponds to the optimal condition (800 W, 200 s DT, 2 layers, 5 mm BT; average residual stress= 98.8 MPa).
- Run 8 (Figure 7(b)) represents one of the highest-stress cases (1200 W, 400 s DT, 4 layers, 3 mm BT; average residual stress= 172.0 MPa).

Under the optimized conditions in Run 9, the maximum uplift at the center of the deposited wall is limited to around +0.112 mm, and the overall deformation profile is smooth and symmetrical, suggesting a well-controlled thermal expansion and contraction process. In comparison, Run 8 shows a maximum vertical displacement of +0.180 mm under larger thermal gradients, with excessive edge deflections and an asymmetrical deformation profile. The lower magnitude and more uniform distribution of U3 in Run 9 confirm that reduced laser power, reduced dwell time, minimized layer count, and increased baseplate thickness are efficient in minimizing distortion in DED-processed SS316L components.

4. CONCLUSIONS

A full factorial experimental design was applied to evaluate the influence of four process parameters—baseplate thickness (BT), dwell time (DT), laser power (P), and layer count (L)—on residual stress in the DED process. The ANOVA results indicated that the selected regression model is statistically robust, with R^2= 99.95%, R^2 adj= 99.92%, and R^2 pred= 99.82%. Among the various parameters examined, baseplate thickness had the most significant individual influence, contributing 8.2% of the overall variability in residual stress. The interaction between baseplate thickness and laser power (BT×P) contributed 1.34%, highlighting a pronounced synergistic effect. In comparison, layer count (L) had a minimal influence (0.003%), and dwell time (DT) and laser power (P) contributed 0.08% and 0.05%, respectively. The interaction L × P had a measurable impact (0.12%), whereas L × DT was marginally non-significant (0.03%). The minimum residual stress was predicted to occur at the highest level of baseplate thickness and the lowest levels of layer count, dwell time, and laser power.

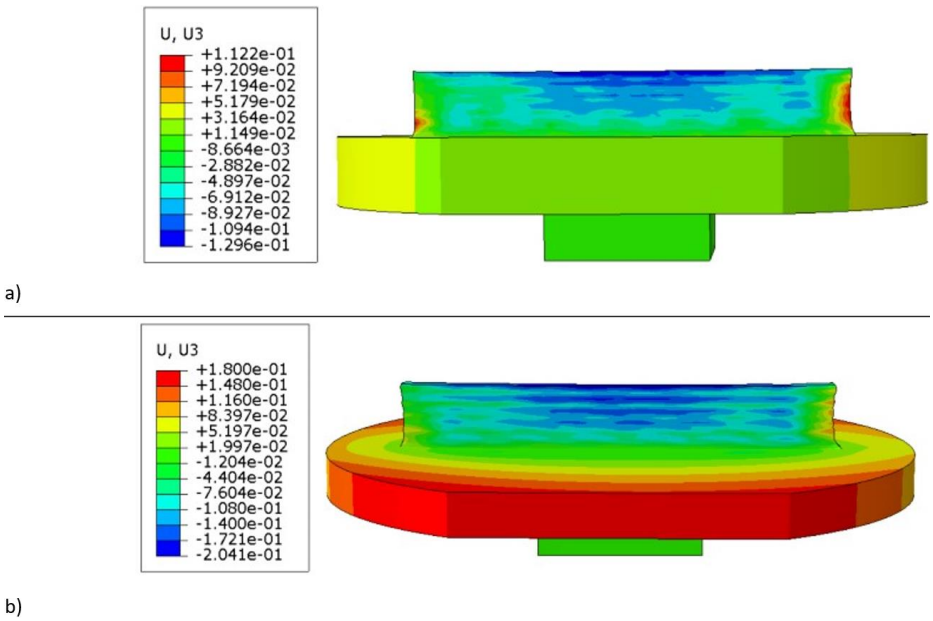

Fig. 7. Vertical displacement (U3) contours for Run 9 a) under optimized conditions and Run 8 b) under high-stress conditions

Additionally, displacement analysis showed a significant increase in vertical distortion when baseplate thickness was reduced from 5 mm to 3 mm, with peak U3 displacement increasing from approximately 0.11 mm to 0.18 mm (63% increase), further demonstrating the mechanical impact of thermal boundary rigidity.

REFERENCES

[1] W. E. Frazier, "Metal additive manufacturing: a review", J. Mater. Eng. Perform., 2014, 23, 1917–1928. doi: 10.1007/s11665-014-0958-z.

[2] J. J. Lewandowski and M. Seifi, "Metal additive manufacturing: a review of mechanical properties", Annu. Rev. Mater. Res., 2016, 46, 151–186. doi: 10.1146/annurev-matsci-070115-032024.

[3] A. L. Vyatskikh et al., "Residual stress mitigation in directed energy deposition", Mater. Sci. Eng. A, 2023, 871, 144845. doi: 10.1016/j.msea.2023.144845.

[4] C. Meier et al., "Thermophysical phenomena in metal additive manufacturing by selective laser melting: fundamentals, modeling, simulation and experimentation", arXiv preprint arXiv: 1709.09510, 2017.

[5] G. Schajer, Practical Residual Stress Measurement Methods, John Wiley & Sons, 2013.

[6] R. D. Adams and D. G. Moffat, "Vibratory stress relief: a fundamental study of effectiveness", J. Eng. Mater. Technol., 1980, 102, 169–176. doi: 10.1115/1.3224793.

[7] K. P. Walker, "Research and development program for nonlinear structural modeling with advanced time-temperature dependent constitutive relationships", Report PWA-5700-50, NASA CR-165533, 1981.

[8] M. R. Eslami and H. Mahbadi, "Load and deformation controlled cyclic loadings", Fourth International Congress on Thermal Stresses, Osaka, Japan, 2001, 11–16.

[9] B. P. Leonard, "Elliptic systems: finite-difference method IV", in Handbook of Numerical Heat Transfer, W. J. Minkowycz, E. M. Sparrow, G. E. Schneider, and R. H. Pletcher, Eds., John Wiley, New York, 1988, 347–378.

[10] J. Goldak, A. Chakravarti, and M. Bibby, "A new finite element model for welding heat sources", Metall. Trans. B, 1984, 15, 299–305. doi: 10.1007/BF02667333.

[11] B. Jelinek et al., "Two-dimensional thermal finite element model of directed energy deposition: matching melt pool temperature profile with pyrometer measurement", arXiv preprint arXiv: 2007.01433, 2020.

[12] N. Grilli et al., "Crystal plasticity model of residual stress in additive manufacturing", arXiv preprint arXiv: 2105.13257, 2021.

[13] X. Liu, X. Liu, and P. Witherell, "A framework for simulating the path-level residual stress in the laser powder bed fusion process", arXiv preprint arXiv: 2407.06293, 2024.

[14] A. H. Mahmoudi et al., "A new procedure to measure near yield residual stresses using the deep hole drilling technique", Exp. Mech., 2009, 49, 595–604. doi: 10.1007/s11340-008-9158-y.

[15] M. Rombouts et al., "Residual stress in selective laser melting: origin, significance and reduction strategies", Rapid Prototyp. J., 2013, 19, 282–290.

[16] J. P. Kruth et al., "Residual stress measurements and modelling in selective laser melting", Rapid Prototyp. J., 2012, 18, 149–159.

[17] M. Shiomi, K. Osakada, K. Nakamura, T. Yamashita, and F. Abe, "Residual stress within metallic model made by selective laser melting process", CIRP Ann. Manuf. Technol., 2004, 53, 195–198. doi: 10.1016/S0007-8506(07)60677-5.

[18] P. Mercelis and J. P. Kruth, "Residual stresses in selective laser sintering and selective laser melting", Rapid Prototyp. J., 2006, 12, 254–265. doi: 10.1108/13552540610707013.

[19] D. Gu, W. Meiners, K. Wissenbach, and R. Poprawe, "Laser additive manufacturing of metallic components: materials, processes and mechanisms", Int. Mater. Rev., 2012, 57, 133–164. doi: 10.1179/1743280411Y.0000000014.

[20] Q. Jia and D. Gu, "Selective laser melting additive manufacturing of Inconel 718 superalloy parts: densification, microstructure and properties", J. Alloys Compd., 2014, 585, 713–721. doi: 10.1016/j.jallcom.2013.09.171.

[21] A. V. Gusarov, M. Pavlov, and I. Smurov, "Residual stresses at laser surface remelting and additive manufacturing", Phys. Procedia, 2011, 12, 248–254. doi: 10.1016/j.phpro.2011.03.032.

[22] Y. Zhang et al., "Functionally graded materials by additive manufacturing: a review", Adv. Eng. Mater., 2018, 20, 1700841. doi: 10.1002/adem.201700841.
[23] Y. Shi et al., "An overview of laser additive manufacturing of metals: principles, advantages and limitations", Int. J. Mach. Tools Manuf., 2015, 89, 1–15.
[24] A. Kiran, J. Hodek, J. Vavřík, M. Urbánek, and J. Džugan, "Numerical simulation development and computational optimization for directed energy deposition additive manufacturing process", Materials, 2020, 13, 2666. doi: 10.3390/ma13112666.
[25] Q. Yang, P. Zhang, L. Cheng, Z. Min, M. Chyu, and A. C. To, "Finite element modeling and validation of thermomechanical behavior of Ti-6Al-4V in directed energy deposition additive manufacturing", Addit. Manuf., 2016, 12, 169–177. doi: 10.1016/j.addma.2016.06.012.